Frontiers in Bioscience Landmark

Front. Biosci. (Landmark Ed) **2026**; 31(8): 53058
https://doi.org/10.31083/FBL53058

Original Research

Dexmedetomidine Mitigates Sepsis-Associated Lung Injury by Suppressing Macrophage Ferroptosis via the Nrf2/HO-1 Signaling Pathway

Bei Ma[1,2,3,†], Renjie Luo[2,3,†], Gang Kuang[2,3,4], Jian Liu[2,3,5], Xi Chen[1,3], Fang Xu[2,3], Yisi Zhao[1,2,3,*]

[1]Department of Critical Care Medicine, Liangjiang Hospital of Chongqing Medical University, 401121 Chongqing, China
[2]Department of Critical Care Medicine, The First Affiliated Hospital of Chongqing Medical University, 400010 Chongqing, China
[3]The Chongqing Key Laboratory of Translational Medicine in Major Metabolic Diseases, The First Affiliated Hospital of Chongqing Medical University, 400010 Chongqing, China
[4]Department of Critical Care Medicine, Dazu Hospital of Chongqing Medical University, 402360 Chongqing, China
[5]Department of Critical Care Medicine, Youyang Hospital, A Branch of The First Affiliated Hospital of Chongqing Medical University, 409800 Chongqing, China
*Correspondence: 476663973@qq.com; zhao14@hospital.cqmu.edu.cn (Yisi Zhao)
[†]These authors contributed equally.
Academic Editor: Esteban C. Gabazza
Submitted: 18 April 2026 Revised: 19 July 2026 Accepted: 23 July 2026 Published: 18 August 2026

Abstract

Background: To investigate the protective role of dexmedetomidine (DEX) in sepsis-associated acute lung injury through the regulation of macrophage ferroptosis. **Methods:** *In silico* screening of GeneCards and FerrDb Vv3 databases was performed to identify ferroptosis-related candidate genes modulated by dexmedetomidineDEX, lung injury, and macrophage activity, prioritizing nuclear factor erythroid 2-related factor 2 (*Nrf2*)/*Nfe2l2* for subsequent experimental validation. A murine cecal ligation and puncture model of acute lung injury (ALI) and lipopolysaccharide-stimulated macrophages were established and subjected to treatment with DEX and/or the Nrf2 inhibitor ML385. Glutathione peroxidase 4 (GPX4), Nrf2, and heme oxygenase-1 (HO-1) protein levels were analyzed using western blotting. Ferroptosis and oxidative stress markers (superoxide dismutase [SOD], glutathione [GSH], iron content, reactive oxygen species [ROS], malondialdehyde [MDA]) were measured. Samples of fresh lung tissue were observed by electron microscopy. Macrophage phenotypes and tumor necrosis factor alpha (TNF-α) expression were assessed. Macrophage-conditioned medium was used to culture non-small cell adenocarcinoma epithelial cells (A549), and cell migration was evaluated. Proliferation-related proteins (matrix metalloprotease 9 [MMP-9] and Snail-1), key tight junction proteins (zonula occludens-1 [ZO-1] and occludin) and the apoptotic status were also analyzed. **Results:** DEX significantly reduced ROS, iron content, and MDA levels while concomitantly increasing SOD activity and GSH content in both ALI model mice and LPS-treated macrophages. DEX inhibited pro-inflammatory M1 macrophage polarization with a concomitant decrease in TNF-α release through Nrf2-dependent mechanisms. DEX was found to mitigate inflammatory microenvironment-induced macrophage ferroptosis through activation of Nrf2 signaling, thereby reducing damage in A549 cells. This effect may be linked to the regulation of macrophage inflammatory phenotypes. **Conclusions:** DEX improved sepsis-associated ALI by inhibiting macrophage ferroptosis and polarization toward the M1 type by activation of the Nrf2/HO-1 pathway.

Keywords: dexmedetomidine; Nrf2; macrophage; ferroptosis; sepsis-associated lung injury

1. Introduction

Sepsis is a serious condition resulting from a dysregulated systemic host response to an infectious agent, ultimately causing severe organ failure that can be fatal [1]. Annually, there are 48.9 million new sepsis cases worldwide, contributing to 19.7% of global mortality [2]. The lungs are highly susceptible to severe immune-related damage in sepsis, which can progress to acute lung injury and respiratory distress syndrome (ALI/ARDS). Cohort study-derived evidence has established ALI as the earliest complication of sepsis and revealed that it is linked to the highest mortality rate, which can reach as high as 60% [3]. Key immunopathological hallmarks of ALI in sepsis involve the overproduction of inflammatory cytokines and aberrant responses of macrophages and other immune cell populations, leading to an exaggerated inflammatory response and damage to the lung tissue [4]. Macrophages play a pivotal role in regulating the fundamental processes of the inflammatory response and the repair of damaged lung tissue in ARDS [5], including macrophage polarization. Resident macrophages within tissues recruit and activate macrophages to release pro-inflammatory cytokines, inducing neutrophil infiltration, which aggravates inflammation, destroys the endothelial barrier, and worsens lung injury [6]. Therefore, investigating the pathogenic mechanisms through which macrophages shape lung damage

represents an important direction for research focused on sepsis-associated ALI [7].

During the development of sepsis, host tissues experience multiple types of cell death, including programmed necrosis, apoptosis, and ferroptosis. This latter form of programmed cell death, first identified in 2012 [8,9], involves lipid peroxidation and membrane iron accumulation within cells, leading to reduced glutathione peroxidase 4 (GPX4) activity and subsequent cell death [10]. Emerging evidence increasingly suggests that ferroptosis significantly contributes to sepsis-associated multi-organ damage [11,12]. Iron overload triggers lipid peroxidation and the proliferation of fibroblasts through its effects on alveolar epithelial cells and neutrophils, thereby intensifying inflammatory responses and triggering lung fibrosis [13]. Experimental models of ALI reported exhibit elevated levels of ferroptotic markers (iron content, reactive oxygen species [ROS], and malondialdehyde) along with decreased glutathione (GSH) levels. Mitigating ferroptosis reduces lung injury [14], demonstrating that targeting ferroptotic activity in immune cells may offer a novel therapeutic approach to ALI treatment [15].

Nuclear factor erythroid 2-related factor 2 (Nrf2) is a core transcription factor that regulates cellular redox homeostasis. Activation of NRF2 upregulates the expression of multiple antioxidant and cytoprotective genes, including heme oxygenase-1 (HO-1) and GPX4, and is considered a key defense pathway against ferroptosis [16]. Studies have shown that activation of the Nrf2 pathway in macrophages—for example, by itaconate derivatives such as 4-octyl itaconate or by naringenin—can inhibit ferroptosis in macrophages themselves, promote their polarization toward the anti-inflammatory M2 phenotype, and reduce the release of pro-inflammatory cytokines, thereby exerting protective effects against lung injury [17,18].

Dexmedetomidine (DEX) is a highly selective agonist at the α2 adrenergic receptor. DEX is prominently found in hematopoietic and immune tissues, where it plays a crucial role in orchestrating the inflammatory immune response [19]. In previous studies, we found that DEX can reduce myeloperoxidase (MPO) and inflammatory cytokine activity to abrogate lung injury in cecal ligation and puncture (CLP) mice [20]. DEX has also been found to modulate macrophage phenotypes [21] and to alleviate the inflammatory activation of nonventilated lung tissues [22]. Notably, DEX can inhibit ferroptosis and protect against tissue damage in the context of renal [23], myocardial [24], and liver [25] injury following renal ischemia/reperfusion. These prior data thus implicate ferroptosis and macrophage polarization as key mechanisms through which DEX may exert its regulatory and protective effects on macrophages in the context of sepsis.

To clarify the effects of DEX on macrophages and the broader immune response in the context of post-septic lung injury, in the present study, we employed a murine CLP model of ALI, in addition to exposing RAW264.7 cells to lipopolysaccharide (LPS). To assess the impact of DEX on macrophage activity and ferroptosis-related pathways, cells were administered DEX, the selective Nrf2 inhibitor ML385, or were left untreated, thus offering additional insight into the role of Nrf2 in DEX-mediated macrophage activity and ferroptosis.

2. Materials and Methods

2.1 Candidate Gene Screening

To gain bioinformatics evidence supporting the notion that Nrf2 is the central mediator linking DEX treatment, sepsis pathophysiology, and ferroptosis, we performed a systematic intervention screening. Genes related to lung injury, DEX, and macrophages were obtained from GeneCards (https://www.genecards.org/, Version 6.1 - June 17, 2026), with a Venn diagram being used to identify overlapping candidate genes. Ferroptosis-related genes were identified through the Ferrdb V3 database (https://www.zhounan.org/ferrdb/v3/pages/index.html, Version FerrDb V3 2025), and their overlap with other candidate genes was similarly evaluated with a Venn diagram, thus establishing a list of ferroptosis-related genes that are also associated with DEX, lung injury, and macrophages.

2.2 Reagents

Dexmedetomidine (Sigma-Aldrich, SML0956); LPS (Sigma-Aldrich, #L2880); ML385 (MCE, Y-100523), RSL3 (Selleck, S8155), Ferroptosis-IN-22 (MCE, HY-175869), FerroOrange (Fe^{2+} indicator) probe (maokangbio, MX4559) and a tumor necrosis factor alpha (TNF-α) enzyme-linked immunosorbent assay (ELISA) kit (4A Biotech, CME0004) were used for this study. Utilized antibodies are detailed in the corresponding Methods sections.

2.3 Animals

Male C57BL/6 mice (6–8 weeks, 18–22 g) were obtained from the Experimental Animal Center of Chongqing Medical University. Mice were maintained in specific pathogen free (SPF)-grade barrier facilities with ad libitum access to sterilized feed and water. The experimental procedures in this project were approved by the Laboratory Animal Management and Use Committee of Chongqing Medical University (IACUC-CQMU-2023-0466) and were in accordance with national regulations and principles concerning animal protection, welfare, and ethics.

2.4 Experimental Animal Treatment

Animals were randomly allocated to experimental groups using a random number table method. Mice were subjected to CLP modeling as described previously [23]. Briefly, the mice were anesthetized with 5% isoflurane for induction and maintained with 2% isoflurane during the surgical procedure, after which a midline abdominal incision was made. The cecum was ligated and punctured with a

22-gauge needle to release a small amount of stool, repositioned, and the wound was closed. The sham group underwent the same procedure without the ligation and puncture steps. Mice were categorized into four groups: sham, CLP, CLP + DEX, and CLP + DEX + ML385. For the CLP group: Mice underwent CLP surgery and received a single intraperitoneal injection of 50 µL PBS at 30 min post-CLP. DEX group: Mice underwent CLP surgery and received a single intraperitoneal injection of dexmedetomidine (50 µg/kg body weight, dissolved in 50 µL PBS) at 30 min post-CLP. For ML385, the relevant group received an intraperitoneal injection of ML385 (30 mg/kg) 30 min before the CLP procedure, and all groups received an equivalent volume of DMSO as a vehicle control, following a well-established dosing regimen from our prior work. Sham group: Mice underwent the same surgical procedure without cecal ligation and puncture, and received an equal volume of PBS at the same time points. All experiments were performed using three independent biological replicates. At the experimental endpoint (24 h post-operation), mice were humanely euthanized for tissue collection. First, mice were anesthetized via inhalation of 5% isoflurane for induction, after which the concentration was maintained at 2%. Subsequently, euthanasia was performed by exposure to 100% medical-grade carbon dioxide (CO_2) in a transparent sealed chamber. CO_2 was introduced at a flow rate that displaced 30% to 70% of the chamber volume per minute, a method recommended to minimize distress. To ensure irreversible death, the exposure to CO_2 was maintained for a minimum of 5 min after the cessation of breathing was observed. Death was confirmed by verifying the absence of a pedal reflex, respiratory arrest, and fixed pupil dilation. The entire lungs were removed, and the coronal tissue characteristics were then observed. Lung and blood samples were collected and stored at –80 °C.

2.5 Lung Wet-to-Dry Ratio Measurement

Twenty-four h after the CLP procedure, mice were euthanized. Lung tissues were extracted and weighed to obtain the wet weight of the lungs. The wet-to-dry ratio (W/D) was then derived by measuring the dry weight of the lungs.

2.6 Cell Culture and Drug Treatment

The murine RAW264.7 cell line (*Mus musculus*-derived male abdominal macrophage cell line; RAW 264.7 [TIB-71], RRID CVCL_0493) was obtained from the Stem Cell Bank of the Chinese Academy of Sciences in October 2022. A549 cells (*Homo sapiens*, male, lung adenocarcinoma; CCL-185, RRID: CVCL_0023) were obtained from the Stem Cell Bank of the Chinese Academy of Sciences in May 2023. Short tandem repeat (STR) profiling was used to authenticate the cell lines, yielding matching rates of 98.2% for RAW264.7 cells against the American Type Culture Collection (ATCC) TIB-71 reference and 99.1% for A549 cells against the ATCC CCL-185 reference, confirming their identity and the absence of cross-contamination according to the International Cell Line Authentication Committee (ICLAC) database. Samples were confirmed to be negative for mycoplasma contamination based on quantitative polymerase chain reaction (qPCR) analysis targeting the mycoplasma 16S rRNA gene.

All cells were cultured in DMEM supplemented with 10% FBS and 1% penicillin/streptomycin (Gibco, USA) under at 37 °C in a humidified atmosphere containing 5% CO_2. Cells were categorized into four groups: Control, LPS, LPS + DEX, and LPS + DEX + ML385. Cells in appropriate groups were treated for 24 h with LPS (100 ng/mL), DEX (1 µM), and/or ML385 (1 µM).

2.7 Ferroptosis Inhibition and Ferroptosis Activation Experiments

To definitively clarify the causal relationship between ferroptosis and macrophage polarization, we performed targeted intervention experiments *in vitro* model using the classical ferroptosis inducer RSL3 and the ferroptosis inhibitor Ferroptosis-IN-22 (Fer-IN-22, MCE, HY-175869). Ferroptosis activator RSL3 (Selleck, S8155) (3 µM, for 6 h) was added on the basis of the LPS+DEX group. The Ferroptosis inhibitor Fer-IN-22 (4 µM, for 6 h) was added as a positive control on the basis of the LPS group.

2.8 qPCR

After treating RAW264.7 cells in the Control, LPS (100 ng/mL), and DEX (1 µM) groups, changes in the expression of key macrophage-related genes were assessed by qPCR. RNAiso+ (Takara, 9109) was used to isolate total RNA from RAW264.7 cells, after which qPCR was performed with a Bio-Rad PCR system (USA) utilizing TB Green™ Premix Ex Taq™ II (Tli RNaseH Plus) from Takara (RR820A). The $2^{-\Delta\Delta Ct}$ method was then used for analysis.

The primer sequences used in this study are listed below:

Nrf2-F: GGCAGAGACATTCCCATTTGTAG, R: TCGCCAAAATCTGTGTTTAAGGT.

Hmox1-F: AAGCCGAGAATGCTGAGTTCA, R: GCCGTGTAGATATGGTACAAGGA.

Nqo1-F: AGGATGGGAGGTACTCGAATC, R: AGGCGTCCTTCCTTATATGCTA.

Gclc-F: TGGCCACTATCTGCCCAATT, R: GTCTGACACGTAGCCTCGGTAA.

Mouse *β-Actin*-F: CACCATGTACCCAGGCATT-3′, R: CAGCTCAGTAACAGTCCGCC-3′.

2.9 Histological Analysis

The right upper lung lobe of each lung was fixed in 4% paraformaldehyde overnight, followed by paraffin embedding, sectioning, and staining with hematoxylin and eosin (H&E). Pathological images were then obtained under an optical microscope. The Mikawa method [26] was employed to evaluate lung injury scores. For histological anal-

ysis, lung injury scoring was performed independently by three researchers blinded to the experimental groups using the Mikawa criteria. The total score was designated as an ALI score.

2.10 Immunohistochemistry

Paraffin-embedded sections underwent deparaffinization, followed by rehydration with a 95% ethanol gradient. Antibodies specific for MPO (Servicebio, GB150006) and TNF-α (Servicebio, GB15188) were applied to tissue sections and incubated overnight at 4 °C, followed by microscopic imaging. Immunohistochemistry (IHC) quantitative analysis was conducted under strictly blinded conditions. For each sample, at least five high-power fields (×400) were randomly captured by a researcher who was unaware of the group allocation. The percentage of positive cells and the staining intensity were independently evaluated by another researcher, also blinded to the sample origin, using ImageJ software. The average value of these five fields was then calculated to represent the final result for each sample.

2.11 Transmission Electron Microscopy

Lung samples (1 mm^3) were promptly fixed in electron microscopy solution after collection. A 1% osmium solution was used for fixation, and samples were dehydrated using an ethanol gradient before being buried and sliced. Mitochondrial ultrastructural characteristics in cells with macrophage-like morphology from lung tissue were then determined by transmission electron microscopy (Hitachi, Japan). For cell identification, we focused on cells with macrophage-like morphology, defined as mononuclear cells containing abundant cytoplasm, irregular cell surface projections, and characteristic cytoplasmic organelles including phagolysosomes and heterogenous vacuoles. Cells exhibiting these morphological features were selected for mitochondrial analysis. At least five randomly selected fields per sample were examined, and the analysis was performed by two independent investigators blinded to group allocation. Representative images showing typical mitochondrial features of ferroptosis (e.g., shrunken mitochondria with increased membrane density, reduced or absent cristae, and outer membrane rupture) were selected for presentation.

2.12 Measurement of GPX4 Enzymatic Activity

Specific GPX4 enzymatic activity was measured using the GPX4 Activity Assay Kit (BC6260, Solarbio, China). Briefly, cells were harvested and lysed to obtain the supernatant. The assay is based on a glutathione reductase-coupled reaction where the oxidation of nicotinamide adenine dinucleotide phosphate (NADPH) is monitored. Samples were incubated with or without a specific GPX4 inhibitor at 37 °C for 1 h. Subsequently, the reaction was initiated by adding the working solution, and the absorbance at 340 nm was monitored over a 5-min period at 25 °C using a UV-spectrophotometer. The specific GPX4 activity was calculated based on the rate of decrease in A340 (representing NADPH consumption) and normalized to the protein concentration (U/mg protein).

2.13 Detection of Fe^{2+} Ions Assay

The contents of Fe^{2+} in RAW264.7 cells were determined according to the manufacturer's instructions. FerroOrange (1 μM, an intracellular Fe^{2+} ions probe, MX4559-24UG; Shanghai Maokang Biotechnology Co.) dispersed in serum-free medium was added to the cells, and cells were incubated for 30 min in a 37 °C incubator, and cells were then collected. Finally, the colocalization of Fe^{2+} fluorescence and cellular bright-field images was observed under a confocal fluorescence microscope (Olympus).

2.14 Lipid Peroxidation MDA Assay

Lipid peroxidation was assessed by measuring MDA levels using Lipid Peroxidation MDA Assay kit (Beyotime, S0131S). Cells are homogenized in PBS or lysis buffer (10% w/v tissue, 0.1 mL per 10^6 cells), centrifuged (10,000–12,000 ×g, 10 min). Protein quantification (bicinchoninic acid [BCA] kit) is recommended for normalization. TBA stock (0.37%) and MDA working solution (freshly prepared) are used. Reaction setup: 0.1 mL sample/standard + 0.2 mL working solution. Incubate at 100 °C for 15 min, cool, centrifuge (1000 ×g, 10 min), and read absorbance at 532 nm (or 530–540 nm). MDA concentration is derived from a standard curve (1–200 μM).

2.15 SOD Analysis

A total SOD assay was used to evaluate the antioxidant capacity and oxidative stress level of tissues and cells. Briefly, 100 μL of the SOD sample preparation solution was added for every 10 mg of lung tissue or 1 × 10^6 cells. The homogenate was centrifuged for 5 min at 12,000 ×g, after which the supernatant was processed as indicated by the manufacturer (Beyotime S0101S).

2.16 Glutathione (GSH) Analysis

A commercial kit (Nanjing Jiancheng Bioengineering A006-2-1) was used to assess GSH as a measure of redox balance and antioxidant activity. Briefly, 20 mg of lung tissue was homogenized in 180 μL of normal saline, while treated cells were lysed in radioimmunoprecipitation assay (RIPA) lysis buffer. The homogenate was then centrifuged at 2500 rpm for 10 min to collect the supernatant, followed by the determination of GSH content.

2.17 Iron Content Detection

Samples of lung tissue (20 mg) and cell precipitates were to be homogenized with lysis buffer using their corresponding commercial kit (Jiancheng Bioengineering, A039-2-1). The lysis buffer was mixed with the test reagent prior to being immersed in boiling water (>95 °C) for five

min. After cooling, samples were centrifuged for 5 min at 3500 rpm to extract the upper layer. Absorption was measured at 520 nm. Iron content was measured with a standard curve.

2.18 Cellular ROS Analyses

Measurement of intracellular ROS production was accomplished using the redox-sensitive fluorescent DCFH-DA probe supplied in a commercial kit (Beyotime, S0033S). Cells were incubated in the dark with DCFH-DA (10 μM) for 30 min and analyzed by flow cytometry. Detection of DCF fluorescence was performed using excitation and emission wavelengths of 488 nm and 525 nm, respectively. Live cells were identified based on FSC/SSC, and the mean fluorescence intensity (MFI) was calculated using a histogram-based approach.

2.19 Enzyme-Linked Immunosorbent Assay (ELISA)

A TNF-α ELISA kit (4 A Biotech, CME0004-F-096) was used to analyze murine serum and cell supernatant samples. Samples were centrifuged at 1000 ×g for 5 min and transferred to the wells of the pre-coated ELISA plate. Subsequent steps were performed based on the provided instructions. Absorbance at 450 nm was recorded using an ELISA plate reader to quantify TNF-α levels.

2.20 Nuclear and Plasma Protein Separation

Detection of Nrf2 nuclear entry was performed as per the protocol provided with the Nuclear and Cytoplasmic Protein Extraction Kit (Beyotime, P0027). Cell precipitates were then combined with pre-cooled cytoplasmic protein extraction reagent A (containing RNase inhibitor), vigorously vortexed, and incubated in an ice bath for 10–15 min. Reagent B was then added, the samples were vortexed, and they were then incubated in an ice bath for 1 min. Following centrifugation at 4 °C (12,000–16,000 ×g, 5 min), the cytoplasmic fraction was retained in the supernatant, while the precipitate was resuspended in nuclear protein extraction reagent, vortexed, incubated in an ice bath for 40 min, and centrifuged to obtain the supernatant containing the nuclear protein fraction.

2.21 Western Blotting

RIPA lysis buffer (Beyotime, P0013B) supplemented with phenyl methyl sulfonyl fluoride (PMSF) and phosphatase inhibitors was employed to extract proteins from lung tissue and cultured cells. The protein concentration in each lysate was measured using a BCA Protein Assay Kit (Beyotime, P0011). The primary antibody was incubated overnight at 4 °C. The primary antibodies used were specific for HO-1 (Proteintech, 66743-1), GPX4 (Proteintech, 67763-1), Nrf2 (Proteintech, 80593-1), inducible nitric oxide synthase (iNOS) (Proteintech, 18985-1-AP), matrix metalloprotease 9 (MMP-9) (Proteintech, 10375-1-AP), and Snail-1 (Proteintech, 13009-1-AP), Occludin (abcam, ab216327), zonula occludens-1 (ZO-1) Polyclonal antibody (proteintech, 21773-1-AP). Horseradish peroxidase (HRP)-conjugated β-Actin (AC028; 1:5000, ABclonal, China; used as a loading control); Anti-glyceraldehyde 3-phosphate dehydrogenase (GAPDH) (ABclonal, 3523011717) and anti-LaminB1 (Proteintech, 12987-1-AP) served as loading controls. HRP-conjugated secondary antibodies (Affinity S0001 and Affinity S0009) were then applied to the membranes for one hour at room temperature. Quantification of protein bands was subsequently performed using a Fusion gel imaging system.

2.22 Immunofluorescence

Immunofluorescence (IF) staining for macrophage phenotypic markers was performed on RAW264.7 cells and paraffin-embedded lung sections. For RAW264.7 cells, following fixation and permeabilization, the cells were blocked with BSA (Servicebio, G1233) and incubated overnight at 4 °C with primary antibodies: mouse monoclonal anti-CD206 (Proteintech, 60143-1-Ig) and rabbit polyclonal anti-iNOS (Proteintech, 22226-1-AP). After washing, the cells were incubated with the corresponding secondary antibodies: FITC-conjugated goat anti-mouse IgG (H+L) (Affinity, #S0007) to detect CD206 (green fluorescence) and Cy5-conjugated goat anti-rabbit IgG (H+L) (Servicebio, GB27303, 1:200) to detect iNOS (red fluorescence).

For lung tissue sections, the samples underwent dewaxing, antigen retrieval, and blocking of endogenous peroxidase activity with 3% hydrogen peroxide prior to BSA blocking. The sections were sequentially incubated with anti-CD206, anti-iNOS, and anti-F4/80 (Servicebio, GB113373, 1:200) using the Tyramide Signal Amplification multiplex method, followed by the application of their corresponding secondary antibodies, with microwave treatment applied between cycles to strip the previously bound antibody complexes.

Finally, all samples were counterstained with 4',6-diamidino-2-phenylindole (DAPI) (Servicebio, G1012) for nuclear visualization, mounted, and the images were captured using a laser confocal microscope.

2.23 Flow Cytometry

Twenty-four hours after CLP-induced mouse model establishment, alveolar lavage fluid (BALF) was collected and centrifuged. Collected cells were stained with FITC anti-mouse CD170 (Siglec-F) (Biolegend, 155504), PE/Cyanine 7 anti-mouse CD11c (Biolegend, 117317), PE anti-mouse CD86 (Biolegend, 105008), and APC anti-mouse CD206 (Biolegend, 141708) for 30 min at 4 °C in the dark. Cells were then analyzed using a flow cytometer. Flow-cytometry gating was established by a researcher blinded to the group assignments, and all samples were analyzed using identical gating parameters through-

out the study. Alveolar macrophages (AM) were identified as Siglec-F+ CD11c+ cells. The ratio of gated CD206+ to CD86+ AMs was then analyzed.

2.24 Conditioned Medium Treatment

A549 cells were treated with 100 ng/mL LPS for 24 h. The culture supernatants from RAW264.7 cells of different experimental groups were subsequently used to stimulate A549 cells for an additional 24 h, including medium from the Control, LPS, LPS + DEX, and LPS + DEX + ML385 groups. A549 cells were then used for downstream analysis. A549 cells were first pre-treated with LPS (100 ng/mL) for 24 h to induce epithelial cell injury. The medium was then removed, and the cells were incubated for an additional 24 h with conditioned medium derived from differentially treated, including medium from the Control, LPS, LPS + DEX, and LPS + DEX + ML385 groups.

2.25 Wound Healing Assay

A549 cells were cultured in 24-well plates until confluent, at which time two cross-shaped wounds were generated in each monolayer using a 200-µL pipette tip. Cells were co-cultured with macrophage-conditioned medium for 48 h. Digital images were captured using an inverted phase-contrast light microscope with a digital camera at 0 and 48 h post-wounding. The distance of cell migration was analyzed using ImageJ. Wound closure (%) = (Initial Scratch Area – Scratch Area at 48 h)/Initial Scratch Area * 100%.

2.26 Flow Cytometry Apoptosis Analyses

A549 cells were harvested for apoptosis analyses performed with an Annexin V-fluorescein isothiocyanate (FITC)/propidium iodide (PI) detection kit (MA0220; Meilunbio), followed by flow cytometry analyses. FlowJo V10 was used for downstream analysis to determine the number of PI+ Annexin V+ late-stage apoptotic cells.

2.27 Statistical Analysis

Data were analyzed using GraphPad Prism 10 (GraphPad Software, USA) and are presented as mean ± SD. All *in vivo* experiments were performed using independent biological replicates (n = 3 animals per group). Assuming a normal distribution a priori for these continuous biological metrics, differences among multiple groups were evaluated using one-way analysis of variance (ANOVA) followed by Tukey's post-hoc test. The effect sizes for key endpoints (specifically, histological analysis and immunohistochemistry [IHC] quantifications) were calculated and reported as Cohen's *d*. A two-sided *p* value < 0.05 was considered statistically significant.

3. Results

3.1 DEX Mitigates CLP-Induced Acute Lung Injury in Mice Via Nrf2

GPX4 plays a crucial role in inhibiting ferroptosis, and DEX was found to enhance pulmonary GPX4 expression in treated mice (Fig. 1a). To gain bioinformatics evidence supporting the notion that Nrf2 is the central mediator linking DEX treatment, sepsis pathophysiology, and ferroptosis, we performed a systematic intervention screening. The GeneCards database was searched for genes related to lung injury, DEX, and macrophages, yielding 6672, 311, and 14907 candidate genes, respectively, including 247 common genes shared among these three categories. A comparison of these 247 genes with ferroptosis-related genes obtained from FerrDb V3 revealed 3 overlapping genes, including *Hmox1*, *Nfe2l2*, *Slc7a11* (Fig. 1b). The Nrf2 protein encoded by the *Nfe2l2* gene serves as a key transcription factor that coordinates cellular antioxidant defenses. During oxidative stress, Nrf2 translocates to the nucleus, whereupon it activates antioxidant genes (e.g., HO-1), diminishes free iron accumulation, and inhibits both lipid peroxidation and ferroptosis [27]. Nrf2 was identified as a putative candidate gene in the above analysis, and qPCR further confirmed an increase in Nrf2 expression in the LPS group, with a further increase observed in the DEX group (Fig. 1c). In murine lung tissue, protein levels of Nrf2 and its downstream target HO-1 were increased by DEX treatment after CLP modeling (Fig. 1d). To test the importance of Nrf2 in this model, the effects of DEX and the Nrf2 inhibitor ML385 on CLP-induced ALI were examined. DEX treatment reduced pathological lung damage as compared to the CLP model group, as evidenced by changes in lung tissue color, the alleviation of pulmonary edema, and the corresponding reduction of lung injury scores (Fig. 1e–g; Cohen's $d = 6.46$). Immunohistochemical staining revealed a significant reduction in MPO (Fig. 1h; Cohen's $d = 4.59$) and TNF-α (Fig. 1i; Cohen's $d = 3.41$) levels in lung tissue after DEX treatment. Furthermore, serum TNF-α levels were markedly reduced after DEX treatment (Fig. 1j). However, these therapeutic effects were partially reversed by ML385 treatment (Cohen's *d* for reversal: lung injury score = 3.27; MPO = 9.02; TNF-α = 3.23). Together, these results suggest that DEX reduces systemic inflammation and ALI in CLP model mice, likely through the enhanced activation of the Nrf2/HO-1 axis.

3.2 DEX Prevents Ferroptosis in Cells With Macrophage-Like Morphology of Lung Through the Nrf2/HO-1 Pathway

DEX treatment was found to increase Nrf2 and HO-1 protein levels, whereas ML385 inhibited this effect (Fig. 2a,b). GPX4 levels in the lungs rose substantially after DEX administration, whereas they decreased in the context of ML385 pretreatment, consistent with the regulation of ferroptosis in lung tissue (Fig. 2c). Consistently, pul-

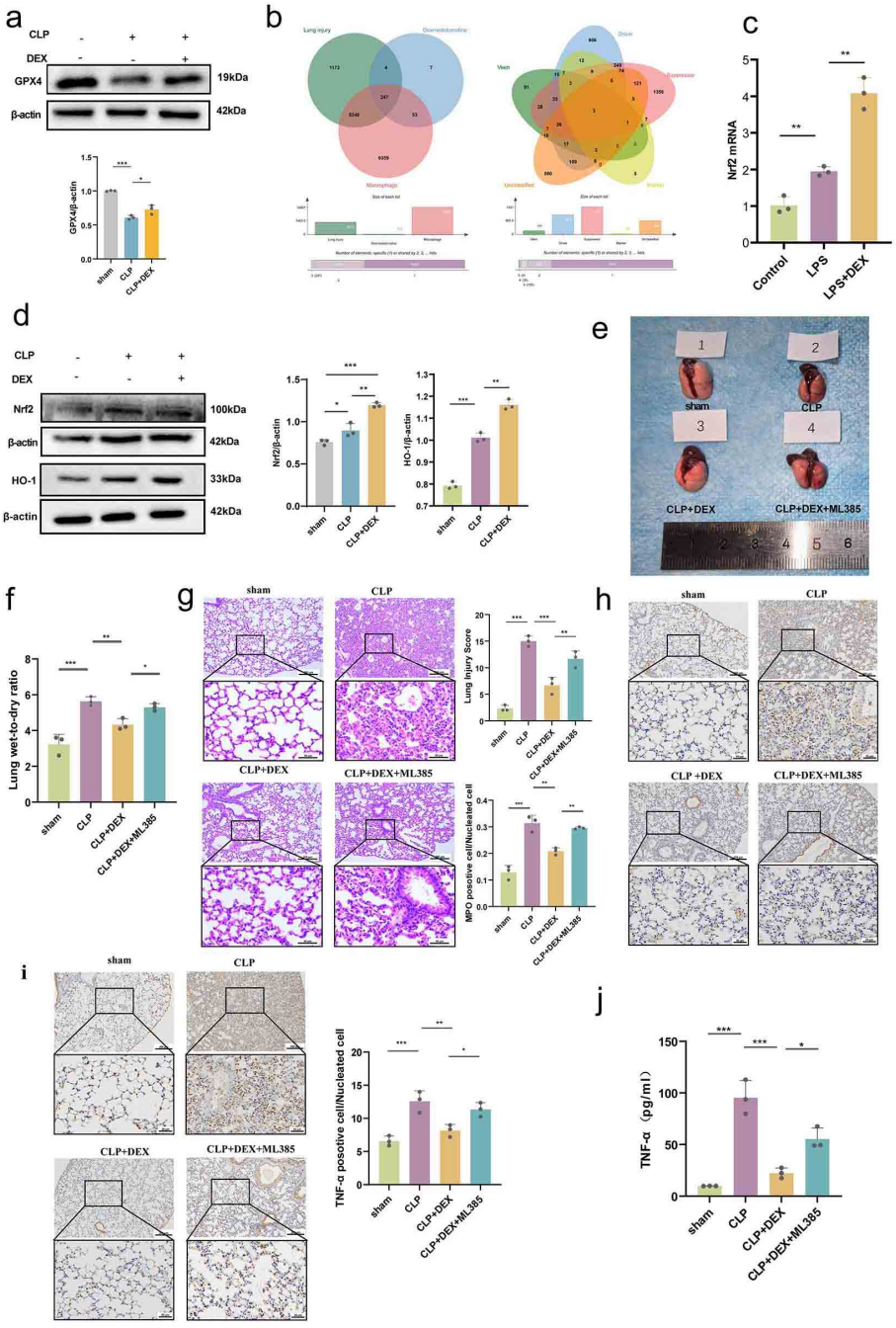

Fig. 1. Dexmedetomidine (DEX) alleviates cecal ligation and puncture (CLP)-induced acute lung injury in mice through nuclear factor erythroid 2-related factor 2 (Nrf2). (a) Western blotting analysis of glutathione peroxidase 4 (GPX4) levels in lung tissue. (b) Venn diagram representation of common candidate target genes. (c) Nrf2 gene expression in RAW 264.7 cells. (d) Western blotting analysis of Nrf2 and heme oxygenase-1 (HO-1) levels in lung tissue. (e) Representative images of murine lung tissues from the indicated experimental groups. (f) Lung wet-to-dry weight ratio (W/D) values. (g) Representative hematoxylin and eosin (H&E) staining images of the lung tissues with corresponding lung injury scores. Upper panel: Low-magnification view showing overall alveolar architecture (scale bar: 200 μm). Lower panel: High-magnification inset highlighting cellular details (scale bar: 50 μm). (h,i) Immunohistochemistry analysis of myeloperoxidase (MPO) and tumor necrosis factor alpha (TNF-α) in lung tissue. Upper panels: Low-magnification views (200×, scale bar: 200 μm) showing overall tissue distribution. Lower panels: High-magnification insets (400×, scale bar: 50 μm) highlighting cellular localization. (j) Murine serum TNF-α concentrations, as measured by enzyme-linked immunosorbent assay (ELISA). n = 3/group. *$p < 0.05$, **$p < 0.01$, ***$p < 0.001$.

monary analyses of ferroptosis-related markers revealed decreased SOD activity and GSH levels in CLP model mice, together with significantly elevated iron content compared to the sham group. DEX restored GSH and SOD activity in treated mice (Fig. 2d,e). In addition, DEX reduced CLP-induced increases in iron content (Fig. 2f). These effects were partially reversed by treatment with ML385. Transmission electron microscopy analysis of lung tissue sections revealed distinct mitochondrial ultrastructural alterations in mononuclear cells with macrophage-like morphology. In the CLP model group, these cells exhibited mitochondrial shrinkage, increased membrane density, reduced or absent cristae, and outer membrane rupture, consistent with features of ferroptosis-associated mitochondrial damage. In the CLP+DEX group, these ferroptotic mitochondrial alterations were notably alleviated, and mitochondrial integrity was partially restored, suggesting a protective effect of DEX on mitochondrial ultrastructure. Co-administration of the Nrf2 inhibitor ML385 partially attenuated the protective effects of DEX, as evidenced by the reappearance of mitochondrial shrinkage, reduced matrix electron density, and disrupted cristae in the CLP+DEX+ML385 group (Fig. 2g). DEX thus appears to exert a regulatory effect on ferroptosis in cells with macrophage-like morphology in lung while this regulatory effect is reversed by the inhibition of Nrf2.

3.3 DEX Mitigates LPS-Triggered Ferroptosis in RAW264.7 Cells Via the Nrf2/HO-1 Signaling Pathway

Electron microscopy results suggested that DEX regulates ferroptosis in cells with macrophage-like morphology of lung tissue. As such, a macrophage inflammation model was established using RAW264.7 cells to explore how LPS-induced ALI correlates with ferroptosis under *in vitro* conditions. The nuclear protein Nrf2 was extracted, and DEX treatment was found to enhance its expression, suggesting an increase in Nrf2 nuclear entry (Fig. 3a), with concomitant upregulation of the downstream protein HO-1 (Fig. 3b). Inhibition of Nrf2 led to a reduction in GPX4 levels (Fig. 3c). An increase in GSH and SOD levels was noted in the DEX group compared with the LPS group (Fig. 3d,e), and DEX significantly reduced the LPS-driven increase in intracellular iron content and MDA levels (Fig. 3f,g). The anti-ferroptotic effects of DEX were partially attenuated by ML385, consistent with our *in vivo* results. To truly reflect the dynamic catalytic kinetics of the enzyme, we determined the enzyme activity of GPX4. The results indicated that following LPS stimulation, GPX4 enzymatic activity was significantly decreased in RAW264.7 (Fig. 3h), whereas DEX intervention effectively restored its catalytic activity. Furthermore, this therapeutic effect was reversed by the co-administration of the Nrf2 inhibitor ML385. To detect intracellular Fe^{2+} with higher specificity we performed live-cell imaging analysis using the FerroOrange probe. DEX treatment reduced intracellular Fe^{2+} fluorescence in LPS-stimulated macrophages, indicating clearance of iron overload. Co-administration of ML385 reversed this effect, restoring high Fe^{2+} signals(Fig. 3i). As highly reactive oxygen-derived compounds produced during oxygen metabolism, ROS play a dynamic regulatory role in shaping ferroptosis, oxidative stress, and inflammatory microenvironments. Flow cytometry was used to assess ROS content based on MFI values, revealing that the LPS-induced rise in ROS levels was ameliorated by DEX treatment, whereas these levels rose again in the ML385 treatment group (Fig. 3j). To confirm that DEX exerts its effects by modulating ferroptosis, we performed additional intervention experiments using the ferroptosis inhibitor Fer-IN-22. Our results showed that under LPS stimulation, the Fer-IN-22 intervention group exhibited a phenotype highly consistent with that of the DEX-treated group. Specifically, GPX4 expression levels were significantly restored(Fig. 3k), MDA accumulation was markedly suppressed(Fig. 3l). The findings demonstrate that DEX suppresses ferroptosis and oxidative stress *in vitro* through the Nrf2/HO-1 pathway.

3.4 DEX Inhibits M1 Macrophages In Vitro and In Vivo Through the Nrf2/HO-1 Pathway

We previously found that changes in the inflammatory microenvironment promote programmed cell death in macrophages [28], with these effects being related to macrophage polarization. As such, we proceeded to investigate the potential of DEX to regulate the inflammatory phenotypic polarization of macrophages via Nrf2. iNOS and CD86 are M1 macrophage markers, whereas CD206 is a marker for the M2 phenotype. Western blotting and IF staining revealed that iNOS expression was enhanced in the LPS group and markedly decreased after DEX administration, whereas it was elevated in response to ML385 treatment *in vitro* (Fig. 4a,b). *In vivo*, bronchoalveolar lavage fluid was isolated from mice and subjected to flow cytometry to quantify surface marker expression on AMs (Siglec-$F^{+}CD11c^{+}$). DEX significantly lowered the proportion of CD86+ cells (Fig. 4c). Lung tissues were collected for immunofluorescence staining to identify interstitial macrophages (IMs, $F4/80^{+}$). The expression of iNOS decreased in the DEX-treated group, whereas it was elevated in the group treated with the Nrf2 inhibitor ML385, while the opposite trend was observed with respect to CD206 expression. Similarly, the effect of DEX on macrophage polarization was partially reversed by ML385 treatment (Fig. 4d). These findings collectively support a role for Nrf2 in these effects, indicating that DEX may impact the inflammatory macrophage microenvironment through Nrf2. Specifically, our central mechanistic conclusions are primarily directed at the AMs population, with the IMs data serving as additional evidence that this Nrf2-dependent regulation extends to the broader pulmonary microenvironment. Consistently, ELISA analyses of super-

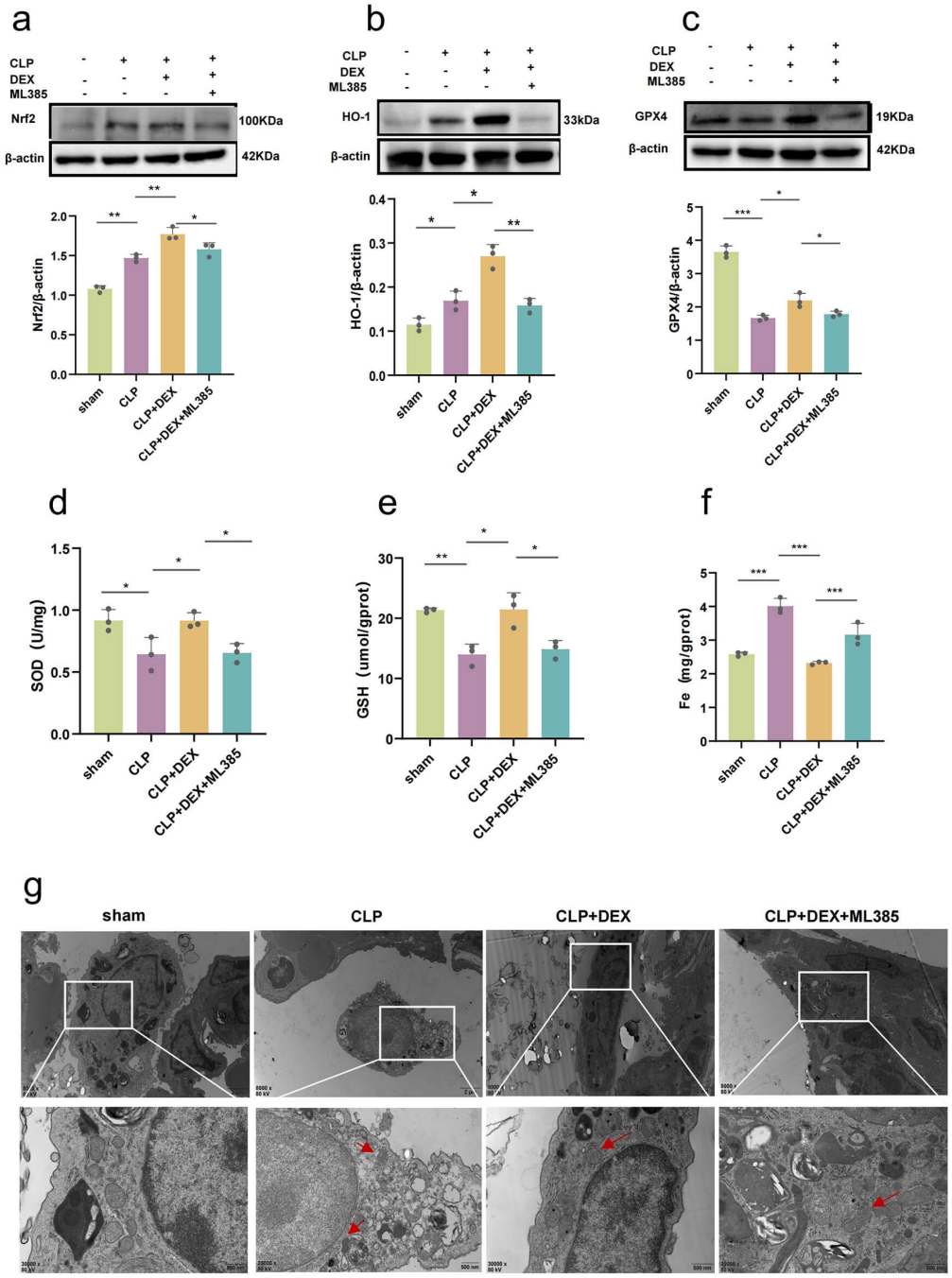

Fig. 2. DEX inhibits lung macrophage ferroptosis in CLP model mice via the Nrf2/HO-1 pathway. (a–c) Western blotting analysis of Nrf2, HO-1, and GPX4 protein levels in lung tissue. (d–f) Superoxide dismutase (SOD) activity and GSH content, and iron content in murine lung tissue. (g) Transmission electron microscopy images of mononuclear cells with macrophage-like morphology in lung tissue samples. The mitochondrial ultrastructure is marked with red arrows. Scale bar: 2 μm (top) and 500 nm (bottom). n = 3/group. *p < 0.05, **p < 0.01, ***p < 0.001.

natants from LPS-stimulated RAW264.7 macrophages revealed that DEX reduces TNF-α levels through Nrf2 activation (Fig. 4e). To definitively clarify the causal relationship between ferroptosis and macrophage polarization, we performed targeted intervention experiments in our *in vitro* model using the classical ferroptosis inducer RSL3 and the ferroptosis inhibitor Fer-IN-22. Under the condition of DEX intervention, the co-administration of RSL3 to reactivate ferroptosis not only re-suppressed GPX4 protein expression but also caused the macrophages to once again exhibit severe intracellular free iron accumulation (indicated by significantly enhanced FerroOrange red fluo-

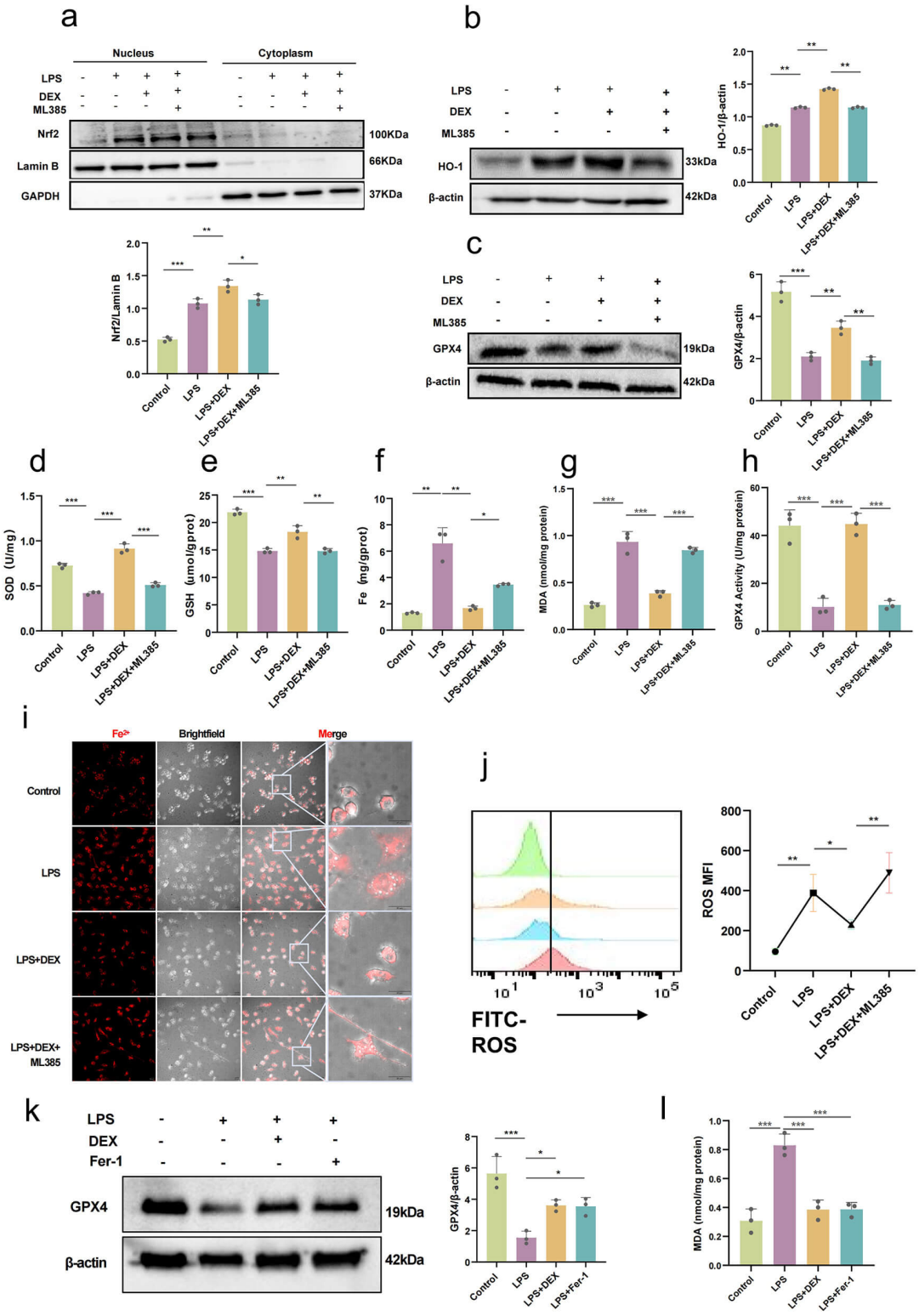

Fig. 3. DEX inhibits LPS-induced ferroptosis in RAW264.7 cells via the Nrf2/HO-1 pathway. (a) Western blotting analysis of nuclear Nrf2 expression. Lamin B and glyceraldehyde 3-phosphate dehydrogenase (GAPDH) were used to identify nuclear and cytoplasmic proteins, respectively. (b,c) Western blotting analysis of HO-1 and GPX4 in RAW264.7 cells. (d–g) SOD, GSH, iron content and MDA level in RAW264.7 cells. (h) The enzyme activity of GPX4. (i) FerroOrange live-cell imaging of intracellular Fe^{2+} in RAW264.7 cells. Scale bar = 20 μm. (j) Flow cytometry-based quantification of reactive oxygen species (ROS) levels. (k) Western blotting analysis of GPX4 in RAW264.7 cells. (l) MDA level in RAW264.7 cells. n = 3/group. $*p < 0.05$, $**p < 0.01$, $***p < 0.001$.

rescence) alongside a typical highly refractive vacuolated morphology. Accompanying this return of the ferroptotic phenotype, the inhibitory effect of DEX on iNOS was reversed, and the macrophages repolarized toward the M1 pro-inflammatory phenotype (Fig. 4f,g).

3.5 DEX Protects Against Epithelial Damage Through the Nrf2-Dependent Disruption of Macrophage Ferroptosis Caused by the Inflammatory Microenvironment

DEX was found to ameliorate macrophage ferroptosis by suppressing pro-inflammatory M1 macrophage polarization-related inflammatory microenvironmental conditions via Nrf2. We next examined the impact of this regulatory effect on pulmonary epithelial-like A549 cells by culturing these injured cells with supernatants from LPS-stimulated RAW264.7 cells and analyzing damage-related phenotypes to evaluate the response of epithelial-like cells to macrophage-derived inflammatory mediators *in vitro* (Fig. 5a). Treating A549 cells with the conditioned medium from DEX-treated RAW264.7 cells was further found to significantly enhance the expression of migration-related Snail1 and MMP-9 (Fig. 5b,c) and ML385 was found to partially abrogate the therapeutic effects of DEX. The expression of tight junction proteins and barrier integrity are more rigorous and standard indicators for assessing epithelial injury in the context of acute lung injury. As shown in the figures, the conditioned medium from LPS-stimulated macrophages significantly downregulated the protein expression of ZO-1 and Occludin, indicating severe epithelial barrier disruption. Conversely, DEX intervention significantly restored the expression of both proteins. Crucially, this protective effect was effectively reversed by the Nrf2 inhibitor ML385 (Fig. 5d,e). What's more, the supernatant from DEX-treated RAW264.7 cells reduced apoptosis in A549 cells (Fig. 5f). The influence of DEX on lung epithelial cell damage was thus found to be mediated by Nrf2-dependent alterations to the composition of the inflammatory microenvironment induced by macrophages.

4. Discussion

DEX is a selective agonist of the α2 adrenergic receptor that enhances lung tissue recovery by modulating macrophage phenotypes and decreasing MPO activity and inflammatory cytokine production [21]. Ferroptosis involves a complex interaction between iron imbalance, fatty acid metabolism, and a weakened antioxidant system [29]. Ferroptosis can trigger a cascading innate immune response, which in turn stimulates inflammation via the secretion of damage-associated molecular patterns [30]. Ferroptosis inhibitors have been demonstrated to ameliorate lung injury [31]. Here, DEX was found to inhibit GPX4/GSH-dependent lipid peroxidation and to significantly inhibit ferroptosis in ALI by reducing excessive ROS accumulation and iron formation.

Prior research indicates that iron overload enhances the expression of M1 markers such as TNF-αand IL-1β, while reducing levels of M2 markers like TGM2. This suggests that ferroptosis influences the polarization of M1 macrophages [32]. The Fenton reaction or GPX4 depletion can catalyze ROS production, promoting M1-type macrophage polarization [33]. M1 macrophages, in turn, secrete cytokines such as TNF-α, which trigger the upregulation of the ACSL3 enzyme, promote intracellular lipid accumulation, and create conditions conducive to ferroptosis [34]. We propose that the phenotypic remodeling of macrophages and ferroptosis interact and contribute to disease progression in CLP-induced ALI by influencing iron metabolism, lipid metabolism, and cytokine secretion [35].

Antioxidant responses are regulated by the transcription factor Nrf2, which plays a crucial role in managing lipid peroxidation and iron metabolism [36]. Activation of the Nrf2/HO-1 pathway promotes M2 macrophage activity and suppresses M1 macrophage activity, thereby reducing inflammation [37]. Our findings suggest that DEX may induce the upregulation and activation of Nrf2/HO-1 and GPX4. Importantly, we verified that neither DEX nor the Nrf2 inhibitor ML385 altered the baseline status of healthy lung tissues and resting macrophages. Furthermore, ML385 administration alone exerted no significant regulatory effects on the lung tissues of CLP mice or LPS-stimulated RAW264.7 cells (**Supplementary Fig. 1**). However, the Nrf2 inhibitor ML385 partially counteracted the effects of DEX. Thus, DEX may inhibit ferroptosis and phenotypic polarization by activating the Nrf2-HO-1 pathway.

In this study, macrophages in the LPS group secreted significantly higher levels of TNF-α, while those in the DEX group secreted significantly lower levels of this inflammatory cytokine. Macrophage-derived secretion of multiple bioactive compounds underpins their modulatory effects on ECs during ALI [38]. During bacterial or viral infections, M1 macrophage polarization leads to significant TNF-α release, enhancing macrophage cytotoxicity or inducing apoptosis in lung epithelial cells [39]. TNF-α promotes macrophage polarization and ferroptosis in some inflammatory diseases [34]. We postulated that macrophage activity and ferroptosis, reflected by elevated TNF-α levels, alter the inflammatory microenvironment, in turn regulating A549 cell migration and death, thereby conferring lung protection.

Although utilizing A549—a lung adenocarcinoma cell line with intrinsic pro-tumor signaling—as a surrogate model for normal alveolar epithelial cells presents distinct limitations, it remains widely recognized and applied in previous literature as a basic *in vitro* model representing the physiological characteristics of alveolar epithelium [40,41]. Specifically, the upregulated expression of Snail-1 and MMP-9, along with the enhanced migration capacity observed in this malignant cell line, more strongly sug-

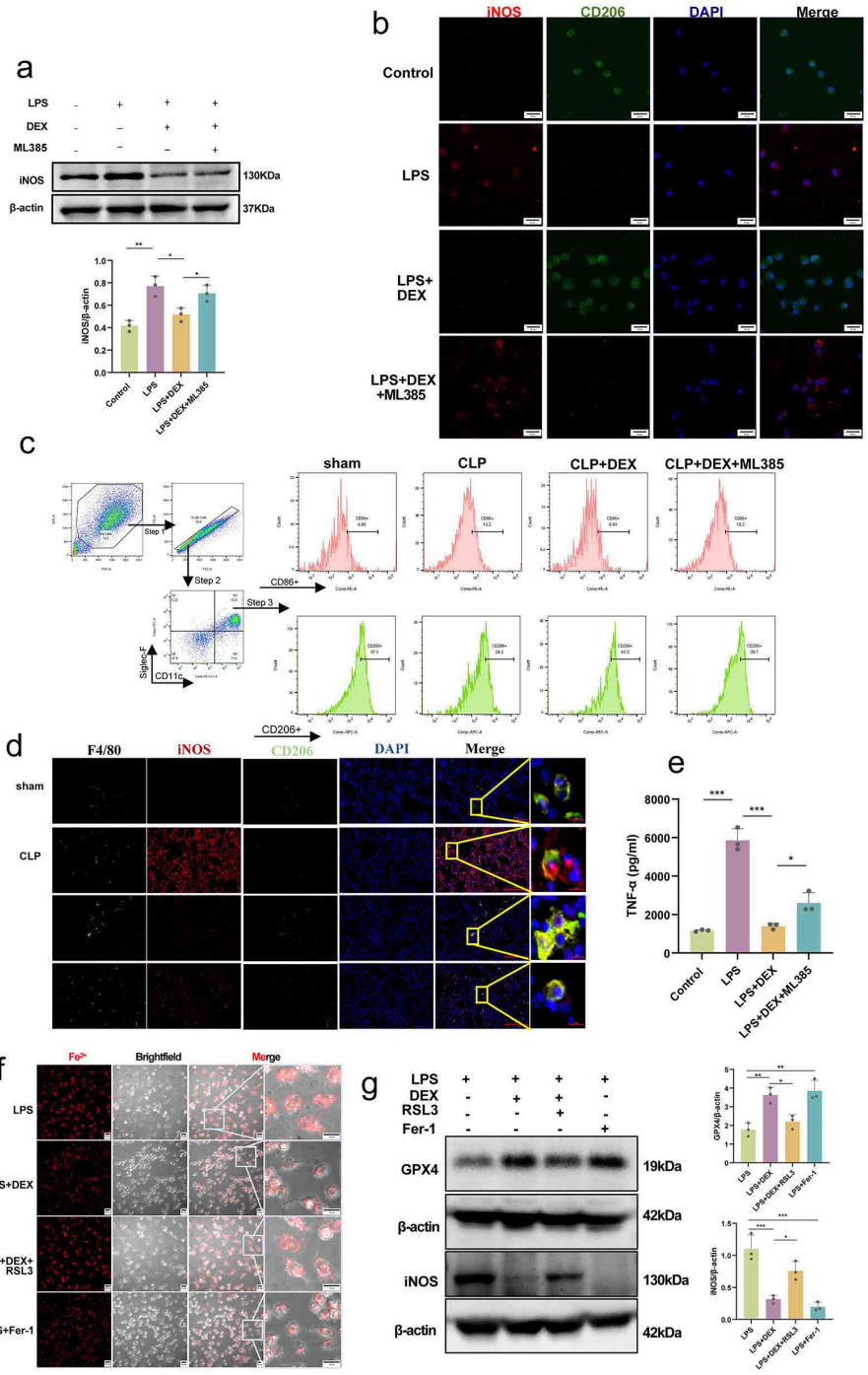

Fig 4. DEX suppresses M1 macrophage responses *in vitro* and *in vivo* via the Nrf2/HO-1 pathway. (a) Western blotting analysis of inducible nitric oxide synthase (iNOS) expression in RAW264.7 cells. (b) Representative immunofluorescence images of iNOS and CD206 in RAW264.7 cells (blue: 4',6-diamidino-2-phenylindole [DAPI], green: CD206, red: iNOS). Scale bar = 50 μm. (c) Flow cytometry-based phenotypic characterization of alveolar macrophages (Siglec-F+ CD11c+), with CD86 being used to identify M1 macrophages and CD206 being used to identify M2 macrophages. (d) Representative fluorescence images of iNOS and CD206 in the lung tissue. F4/80: macrophages (blue: DAPI, green: CD206, red: iNOS, orange: F4/80).Scale bar = 50 μm (main images); Scale bar = 20 μm (enlarged image). (e) ELISA analysis of TNF-α levels in RAW264.7 cell-conditioned medium. (f) FerroOrange live-cell imaging of intracellular Fe^{2+} in RAW264.7 cells. Scale bar = 20 μm. (g) Western blotting analysis of GPX4 and iNOS in RAW264.7 cells. n = 3/group. *$p < 0.05$, **$p < 0.01$, ***$p < 0.001$.

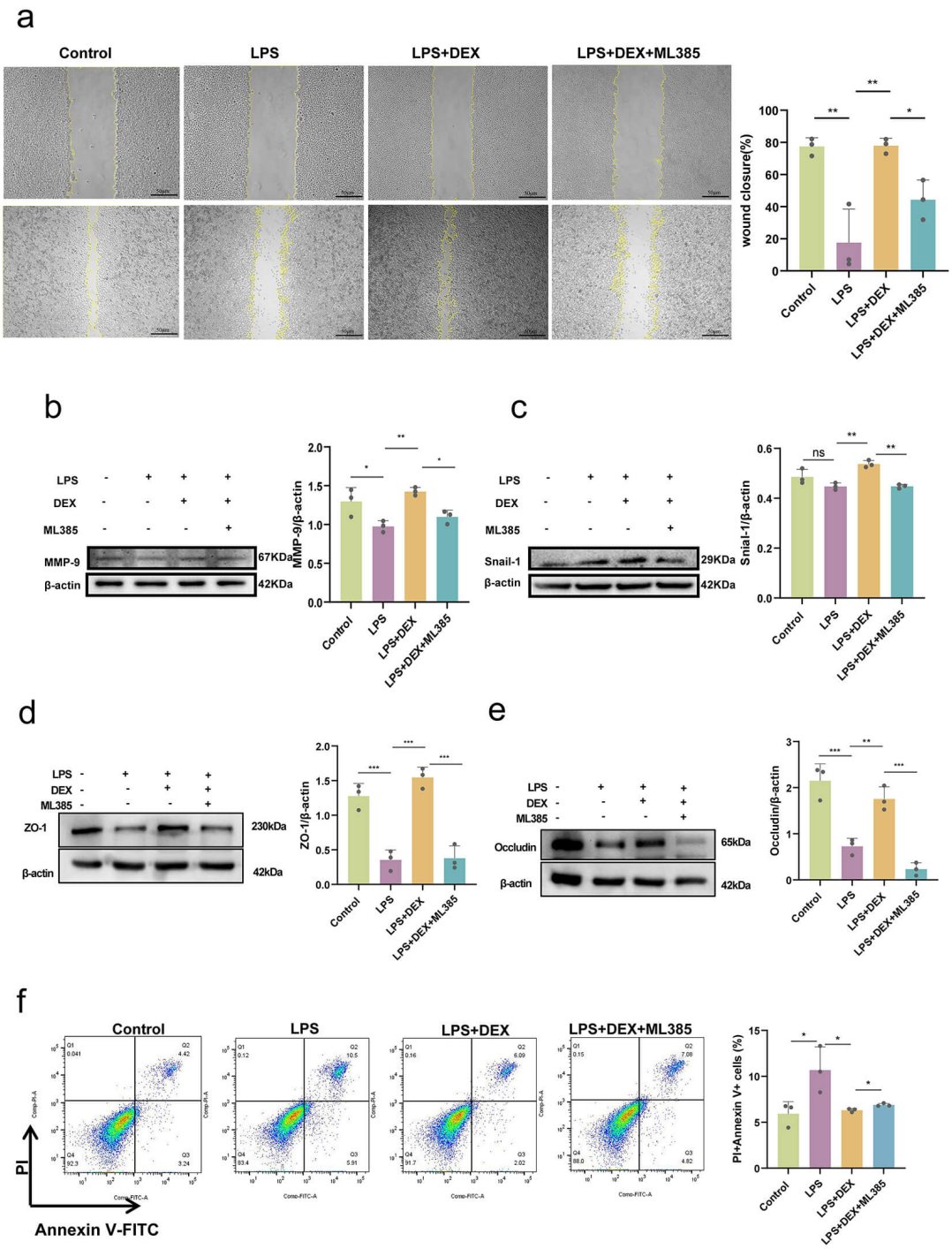

Fig. 5. DEX protects against epithelial damage through the Nrf2-dependent disruption of macrophage ferroptosis caused by the inflammatory microenvironment. (a) A549 cell migration was assessed through a wound healing assay in which A549 cells were treated with conditioned medium from RAW 264.7 cells for 48 h. Yellow lines denote the edges of the wound area (scale bar: 50 μm). Wound closure (%) = (Initial Scratch Area – Scratch Area at 48 h)/Initial Scratch Area × 100%. (b–e) Western blotting analysis of matrix metalloprotease 9 (MMP-9), Snail-1, zonula occludens-1 (ZO-1) and Occludin levels in A549 cells. (f) Annexin V-fluorescein Isothiocyanate (FITC)/propidium iodide(PI) staining and flow cytometry were used to assess A549 cell apoptosis. PI labeling is shown on the Y-axis, while Annexin-FITC labeling is shown on the X-axis. n = 3/group. *$p < 0.05$, **$p < 0.01$, ***$p < 0.001$.

gests pro-tumor signaling (such as epithelial-mesenchymal transition, EMT) rather than simply reflecting normal epithelial injury repair. To address this gap, we additionally performed Western blot analyses for the key tight junction

proteins ZO-1 and Occludin. Nevertheless, given the distinct tumor biological background inherent to this cell line, these key findings must be further validated in parallel using non-malignant epithelial cell lines (e.g., BEAS-2B) or primary alveolar epithelial cells in future studies.

Limitations

Several limitations of this study should be explicitly acknowledged. First, regarding the underlying mechanisms, while DEX was found to inhibit ferroptosis through GSH/GPX4 dependence, further studies are needed to clarify how DEX interacts with phospholipid substrates and iron metabolism. Second, concerning the *in vivo* experimental design, the current study employed a prophylactic treatment regimen in which DEX was delivered concurrently with the septic insult, thereby limiting the direct extrapolation of our findings to clinical scenarios involving established sepsis with delayed therapeutic intervention. Further studies utilizing a therapeutic time window (e.g., DEX administration at 6 h post-CLP) are warranted to validate the translational relevance. Moreover, we must explicitly acknowledge that the specific pharmacological doses of DEX and ML385 used in this murine model cannot be directly extrapolated to human clinical dosing, necessitating future translational pharmacokinetic validations. Furthermore, all *in vivo* measurements were performed at a single time point 24 h post-CLP. Consequently, the distinct kinetics of Nrf2 activation, macrophage polarization, and ferroptosis execution, as well as their precise causal sequence, could not be fully delineated. A systematic short-term kinetic study (e.g., with sampling at 6, 12, 24, and 48 h post-CLP) is necessary to clarify the temporal hierarchy and establish definitive causal relationships. Additionally, relying on the classical M1/M2 dichotomy to evaluate macrophage polarization is an inherent oversimplification, as it does not fully capture the complex and continuous spectrum of macrophage activation states present *in vivo*. Furthermore, our *in vivo* experiments exclusively utilized male mice; future studies must include both sexes to evaluate potential sex bias. Additionally, the potential confounding immunomodulatory effects of isoflurane anesthesia during the procedures cannot be entirely ruled out. Third, from a methodological standpoint, while we have now supplemented the study with adequately powered survival and clinical severity analyses (**Supplementary Fig. 2**, n = 10), the sample sizes for specific downstream targeted mechanistic endpoints (e.g., Western blotting, flow cytometry, and histological evaluations) remained limited (n = 3 independent animals per group). This limited sample size mathematically precludes empirical normality testing and serves as an explicit constraint on robust statistical inference. Although our post-hoc analyses demonstrated extremely large effect sizes (Cohen's $d > 3.0$) for key endpoints such as histological lung injury scores and MPO expression—thereby mathematically supporting the massive biological magnitude of the observed differences despite the small n—future investigations utilizing larger animal cohorts are warranted to completely validate these statistical findings. Finally, our *in vitro* experiments utilized the A549 cancer cell line as a surrogate for alveolar epithelium, and the disruption of Nrf2 relied on a pharmacological agent (ML385). Future validation employing primary alveolar epithelial cells and precise genetic approaches (e.g., Nrf2 knockout models) will be crucial to definitively confirm these regulatory axes.

5. Conclusions

In summary, these results highlight the ability of DEX to prevent inflammation, oxidative stress, and lung injury in sepsis-associated ALI through regulatory effects on macrophages. These effects may be associated with changes in the inflammatory microenvironment induced by the modulation of macrophage inflammatory phenotypes.

Availability of Data and Materials

The data that support the findings of this study are available on request from the corresponding author (476663973@qq.com).

Author Contributions

The experimental design was completed by BM, RL, FX and YZ. BM, RL, GK, JL, XC and YZ are responsible for all experimental operations and data analysis. The manuscript was jointly finished by BM and RL. The manuscript was finally revised by YZ. All authors contributed to editorial changes in the manuscript. All authors read and approved the final manuscript. All authors have participated sufficiently in the work and agreed to be accountable for all aspects of the work.

Ethics Approval and Consent to Participate

The experimental procedures involved in this project have been reviewed by the Laboratory Animal Management and Use Committee of Chongqing Medical University (IACUC-CQMU-2023-0466), and it complies with the principles of animal protection, animal welfare and ethics, as well as the relevant national regulations on the welfare and ethics of laboratory animals. All animal experimental procedures were conducted in accordance with the principles of the 3Rs (Replacement, Reduction, and Refinement), and the study was reported following the ARRIVE guidelines for animal research.

Acknowledgment

Not applicable.

Funding

Sponsored by Natural Science Foundation of Chongqing, China (CSTB2025NSCQ-GPX1219 to YS Zhao); the China Postdoctoral Science Founda-

tion (2025MD784155 to YS Zhao); 2023 Chongqing Science and Health Joint Medical Research Project (2023QNXM005 to Bei Ma); 2022 Chongqing Science and Health Joint Medical Research Project (2022QNXM010 to J Liu).

Conflicts of Interest

The authors declare no conflicts of interest.

Supplementary Material

Supplementary material associated with this article can be found, in the online version, at https://doi.org/10.31083/FBL53058.

References

[1] Weiss SL, Peters MJ, Oczkowski SJW, Belley-Cote E, Buysse C, Choong KLM, et al. Surviving Sepsis Campaign International Guidelines for the Management of Sepsis and Septic Shock in Children 2026. Pediatric Critical Care Medicine. 2026; 27: 379–434. https://doi.org/10.1097/PCC.0000000000003927

[2] GBD 2021 Global Sepsis Collaborators (2025). Global, regional, and national sepsis incidence and mortality, 1990-2021: a systematic analysis. The Lancet. Global Health. 2025; 13: e2013–e2026. https://doi.org/10.1016/S2214-109X(25)00356-0

[3] da Cruz MR, Azambuja P, Torres KSC, Lima-Setta F, Japiassú AM, Medeiros DM. Identification and validation of respiratory subphenotypes in patients with COVID-19 acute respiratory distress syndrome undergoing prone position. Annals of Intensive Care. 2025; 15: 16. https://doi.org/10.1186/s13613-024-01417-9

[4] Zhu W, Zhang Y, Wang Y. Immunotherapy strategies and prospects for acute lung injury: Focus on immune cells and cytokines. Frontiers in Pharmacology. 2022; 13: 1103309. https://doi.org/10.3389/fphar.2022.1103309

[5] Wang W, Zhu L, Li H, Ren W, Zhuo R, Feng C, et al. Alveolar macrophage-derived exosomal tRF-22-8BWS7K092 activates Hippo signaling pathway to induce ferroptosis in acute lung injury. International Immunopharmacology. 2022; 107: 108690. https://doi.org/10.1016/j.intimp.2022.108690

[6] Park I, Kim M, Choe K, Song E, Seo H, Hwang Y, et al. Neutrophils disturb pulmonary microcirculation in sepsis-induced acute lung injury. The European Respiratory Journal. 2019; 53: 1800786. https://doi.org/10.1183/13993003.00786-2018

[7] Tang J, Shi J, Han Z, Chen X. Application of Macrophage Subtype Analysis in Acute Lung Injury/Acute Respiratory Distress Syndrome. Frontiers in Bioscience (Landmark edition). 2024; 29: 412. https://doi.org/10.31083/j.fbl2912412

[8] Yan HF, Zou T, Tuo QZ, Xu S, Li H, Belaidi AA, et al. Ferroptosis: mechanisms and links with diseases. Signal Transduction and Targeted Therapy. 2021; 6: 49. https://doi.org/10.1038/s41392-020-00428-9

[9] Zhang W, Lu J, Wang Y, Sun P, Gao T, Xu N, et al. Canagliflozin Attenuates Lipotoxicity in Cardiomyocytes by Inhibiting Inflammation and Ferroptosis through Activating AMPK Pathway. International Journal of Molecular Sciences. 2023; 24: 858. https://doi.org/10.3390/ijms24010858

[10] Yin X, Zhu G, Wang Q, Fu YD, Wang J, Xu B. Ferroptosis, a New Insight Into Acute Lung Injury. Frontiers in Pharmacology. 2021; 12: 709538. https://doi.org/10.3389/fphar.2021.709538

[11] Li J, Lu K, Sun F, Tan S, Zhang X, Sheng W, et al. Panaxydol attenuates ferroptosis against LPS-induced acute lung injury in mice by Keap1-Nrf2/HO-1 pathway. Journal of Translational Medicine. 2021; 19: 96. https://doi.org/10.1186/s12967-021-02745-1

[12] Wang J, Zhang F, Tan C, Wang N, Xia X, Ye Y, et al. The VDAC3/DHODH Axis Ameliorates Sepsis-induced Myocardial Injury by Regulating Ferroptosis. Frontiers in Bioscience (Landmark edition). 2025; 30: 39559. https://doi.org/10.31083/FBL39559

[13] Deschemin JC, Mathieu JRR, Zumerle S, Peyssonnaux C, Vaulont S. Pulmonary Iron Homeostasis in Hepcidin Knockout Mice. Frontiers in Physiology. 2017; 8: 804. https://doi.org/10.3389/fphys.2017.00804

[14] Qu M, Zhang H, Chen Z, Sun X, Zhu S, Nan K, et al. The Role of Ferroptosis in Acute Respiratory Distress Syndrome. Frontiers in Medicine. 2021; 8: 651552. https://doi.org/10.3389/fmed.2021.651552

[15] Yu T, Sun S. Role and mechanism of ferroptosis in acute lung injury. Cell Cycle (Georgetown, Tex.). 2023; 22: 2119–2129. https://doi.org/10.1080/15384101.2023.2278328

[16] Chen J, Lu X, Liu S, Hu W, Zhou X, Wang Z. Betaine Inhibits Ferroptosis After Intracerebral Hemorrhage by Activating the Nrf2/HO-1 Pathway. Antioxidants (Basel, Switzerland). 2026; 15: 135. https://doi.org/10.3390/antiox15010135

[17] He R, Liu B, Xiong R, Geng B, Meng H, Lin W, et al. Itaconate inhibits ferroptosis of macrophage via Nrf2 pathways against sepsis-induced acute lung injury. Cell Death Discovery. 2022; 8: 43. https://doi.org/10.1038/s41420-021-00807-3

[18] Zhang H, Wang Y, Wang S, Xue X, Huang K, Xu D, et al. Tangeretin alleviates sepsis-induced acute lung injury by inhibiting ferroptosis of macrophage via Nrf2 signaling pathway. Chinese Medicine. 2025; 20: 11. https://doi.org/10.1186/s13020-025-01063-8

[19] Meng L, Li L, Lu S, Li K, Su Z, Wang Y, et al. The protective effect of dexmedetomidine on LPS-induced acute lung injury through the HMGB1-mediated TLR4/NF-κB and PI3K/Akt/mTOR pathways. Molecular Immunology. 2018; 94: 7–17. https://doi.org/10.1016/j.molimm.2017.12.008

[20] Zhang ZT, Xie K, Luo RJ, Zhang DY, He ZW, Li KF, et al. Dexmedetomidine alleviates acute lung injury by promoting Tregs differentiation via activation of AMPK/SIRT1 pathway. Inflammopharmacology. 2023; 31: 423–438. https://doi.org/10.1007/s10787-022-01117-5

[21] Zhou H, Sun J, Zhong W, Pan X, Liu C, Cheng F, et al. Dexmedetomidine preconditioning alleviated murine liver ischemia and reperfusion injury by promoting macrophage M2 activation via PPARγ/STAT3 signaling. International Immunopharmacology. 2020; 82: 106363. https://doi.org/10.1016/j.intimp.2020.106363

[22] Shen Q, Xu G, Liu J, Wang L, Zhou Y, Yu Y, et al. Dexmedetomidine alleviates non-ventilation associated lung injury via modulating immunology phenotypes of macrophages. Life Sciences. 2020; 259: 118249. https://doi.org/10.1016/j.lfs.2020.118249

[23] Tao WH, Shan XS, Zhang JX, Liu HY, Wang BY, Wei X, et al. Dexmedetomidine Attenuates Ferroptosis-Mediated Renal Ischemia/Reperfusion Injury and Inflammation by Inhibiting ACSL4 *via* α2-AR. Frontiers in Pharmacology. 2022; 13: 782466. https://doi.org/10.3389/fphar.2022.782466

[24] Wang Z, Yao M, Jiang L, Wang L, Yang Y, Wang Q, et al. Dexmedetomidine attenuates myocardial ischemia/reperfusion-induced ferroptosis via AMPK/GSK-3β/Nrf2 axis. Biomedicine & Pharmacotherapy = Biomedecine & Pharmacotherapie. 2022; 154: 113572. https://doi.org/10.1016/j.biopha.2022.113572

[25] Zhang Y, Wei H, Wang M, Yu Y, Gu M, Zhong H, et al. Dexmedetomidine alleviates ferroptosis following hepatic ischemia-reperfusion injury by upregulating Nrf2/GPx4-dependent antioxidant responses. Biomedicine & Pharmacother-

apy = Biomedecine & Pharmacotherapie. 2023; 169: 115915. https://doi.org/10.1016/j.biopha.2023.115915

[26] Mikawa K, Nishina K, Takao Y, Obara H. ONO-1714, a nitric oxide synthase inhibitor, attenuates endotoxin-induced acute lung injury in rabbits. Anesthesia and Analgesia. 2003; 97: 1751–1755. https://doi.org/10.1213/01.ANE.0000086896.90343.13

[27] Hu Q, Zuo T, Deng L, Chen S, Yu W, Liu S, et al. β-Caryophyllene suppresses ferroptosis induced by cerebral ischemia reperfusion via activation of the NRF2/HO-1 signaling pathway in MCAO/R rats. Phytomedicine: International Journal of Phytotherapy and Phytopharmacology. 2022; 102: 154112. https://doi.org/10.1016/j.phymed.2022.154112

[28] Kuang G, Zhao Y, Wang L, Wen T, Liu P, Ma B, et al. Astragaloside IV Alleviates Acute Hepatic Injury by Regulating Macrophage Polarization and Pyroptosis via Activation of the AMPK/SIRT1 Signaling Pathway. Phytotherapy Research: PTR. 2025; 39: 733–746. https://doi.org/10.1002/ptr.8403

[29] Oh M, Jang SY, Lee JY, Kim JW, Jung Y, Kim J, et al. The lipoprotein-associated phospholipase A2 inhibitor Darapladib sensitises cancer cells to ferroptosis by remodelling lipid metabolism. Nature Communications. 2023; 14: 5728. https://doi.org/10.1038/s41467-023-41462-9

[30] Tang D, Kroemer G. Ferroptosis. Current Biology: CB. 2020; 30: R1292–R1297. https://doi.org/10.1016/j.cub.2020.09.068

[31] Lai K, Song C, Gao M, Deng Y, Lu Z, Li N, et al. Uridine Alleviates Sepsis-Induced Acute Lung Injury by Inhibiting Ferroptosis of Macrophage. International Journal of Molecular Sciences. 2023; 24: 5093. https://doi.org/10.3390/ijms24065093

[32] Handa P, Thomas S, Morgan-Stevenson V, Maliken BD, Gochanour E, Boukhar S, et al. Iron alters macrophage polarization status and leads to steatohepatitis and fibrogenesis. Journal of Leukocyte Biology. 2019; 105: 1015–1026. https://doi.org/10.1002/JLB.3A0318-108R

[33] Zhou Y, Que KT, Zhang Z, Yi ZJ, Zhao PX, You Y, et al. Iron overloaded polarizes macrophage to proinflammation phenotype through ROS/acetyl-p53 pathway. Cancer Medicine. 2018; 7: 4012–4022. https://doi.org/10.1002/cam4.1670

[34] Jung HS, Shimizu-Albergine M, Shen X, Kramer F, Shao D, Vivekanandan-Giri A, et al. TNF-α induces acyl-CoA synthetase 3 to promote lipid droplet formation in human endothelial cells. Journal of Lipid Research. 2020; 61: 33–44. https://doi.org/10.1194/jlr.RA119000256

[35] Yang Y, Wang Y, Guo L, Gao W, Tang TL, Yan M. Interaction between macrophages and ferroptosis. Cell Death & Disease. 2022; 13: 355. https://doi.org/10.1038/s41419-022-04775-z

[36] Dodson M, Castro-Portuguez R, Zhang DD. NRF2 plays a critical role in mitigating lipid peroxidation and ferroptosis. Redox Biology. 2019; 23: 101107. https://doi.org/10.1016/j.redox.2019.101107

[37] Landis RC, Quimby KR, Greenidge AR. M1/M2 Macrophages in Diabetic Nephropathy: Nrf2/HO-1 as Therapeutic Targets. Current Pharmaceutical Design. 2018; 24: 2241–2249. https://doi.org/10.2174/1381612824666180716163845

[38] Xiong S, Hong Z, Huang LS, Tsukasaki Y, Nepal S, Di A, et al. IL-1β suppression of VE-cadherin transcription underlies sepsis-induced inflammatory lung injury. The Journal of Clinical Investigation. 2020; 130: 3684–3698. https://doi.org/10.1172/JCI136908

[39] Zhao H, Chen Q, Huang H, Suen KC, Alam A, Cui J, et al. Osteopontin mediates necroptosis in lung injury after transplantation of ischaemic renal allografts in rats. British Journal of Anaesthesia. 2019; 123: 519–530. https://doi.org/10.1016/j.bja.2019.05.041

[40] Cooper JR, Abdullatif MB, Burnett EC, Kempsell KE, Conforti F, Tolley H, et al. Long Term Culture of the A549 Cancer Cell Line Promotes Multilamellar Body Formation and Differentiation towards an Alveolar Type II Pneumocyte Phenotype. PloS One. 2016; 11: e0164438. https://doi.org/10.1371/journal.pone.0164438

[41] Xie WM, Su W, Liu XY, Zhou J, Wang M, Wang Y, et al. FTO Deficiency Alleviates LPS-induced Acute Lung Injury by TXNIP/NLRP3-mediated Alveolar Epithelial Cell Pyroptosis. American Journal of Respiratory Cell and Molecular Biology. 2024; 70: 351–363. https://doi.org/10.1165/rcmb.2023-0251OC